RSC Advances

PAPER

View Article Online
View Journal | View Issue

Cite this: *RSC Adv.*, 2024, **14**, 28984

Salt-resistant continuous solar evaporation composites based on nonwovens with synergistic photothermal effect of graphene oxide/copper sulphide†

Wenbo Sun,[ab] Huan Qi,[*bc] Tan Li,[ab] Minggang Lin,[ab] Chuyang Zhang[ab] and Yiping Qiu[bc]

Solar interfacial evaporation is an innovative and environmentally friendly technology for producing freshwater from seawater. However, current interfacial evaporators are costly to manufacture, have poor tolerance to environmental conditions, exhibit instability in evaporation efficiency in highly saline solutions, and fail to prevent salt crystallization. The production of user-friendly, durable and salt-resistant interfacial evaporators remains a significant challenge. By spraying graphene oxide on a nonwoven material using PVA as a binder and adding biphasic Cu_xS by an *in situ* growth method, we designed 2D/3D micro- and nanostructured graphene oxide nanosheets/copper sulfide nanowires (GO/Cu_xS) with synergistic photo-thermal effects in the full spectral range. The evaporation efficiency in pure water was 94.61% with an evaporation rate of 1.5622 kg m^{-2} h^{-1}. In addition, we enhanced convection by employing a vertically aligned water-guide rod structure design, where the concentration difference drives salt dissolution thereby reducing the formation of salt crystals. The evaporation efficiency in 20% salt water was 80.41% with an evaporation rate of 1.3228 kg m^{-2} h^{-1} and long-term stability of brine evaporation was demonstrated under continuous sunlight. This solar steam generator expands the potential application areas of desalination and wastewater purification.

Received 19th July 2024
Accepted 5th September 2024

DOI: 10.1039/d4ra05241b

rsc.li/rsc-advances

1 Introduction

With the rapid industrialization of today's societies, significant amounts of freshwater resources are being consumed and depleted. Seawater is abundant, with total water reserves on Earth of approximately 1386 million cubic kilometers, of which seawater accounts for approximately 97%.[1–3] Seawater desalination can be a viable solution to the issue of water scarcity. The primary method for producing fresh water from seawater is reverse osmosis. The equipment used in this process demonstrates a high level of automation, stable efficiency, purity and other characteristics.[4–8] However, the reverse osmosis process is very energy-intensive. High-temperature, high-energy consumption equipment is required, and the membrane has a short service life. Therefore, it is necessary to develop sustainable and low-cost desalination technologies. Among these, interfacial solar distillation is a promising sustainable technology that converts abundant solar energy into clean water.[9–12]

Many researchers have focused on the development of highly efficient photothermal materials and advanced evaporation structures, including carbon-based materials,[13–17] biomass materials,[18–23] polymers,[24–27] metal–semiconductor materials,[28–31] and natural mineral materials.[32–34] Due to their high energy conversion efficiency and sophisticated functional design for solar energy distillation, organic–inorganic composite materials have garnered significant attention in recent years.[35–37] These two components are typically used as a solar absorber and insulator, respectively, to achieve synergistic photothermal enhancement.[38] Gold nanoparticles (AuNPs) have been widely used in solar evaporation due to the surface plasmon resonance effect.[39] Zheng *et al.* designed colloidal plasma AuNPs capped with ligands of different types and surface coverage densities (*i.e.*, purified and unpurified oleylamine-capped or thiol-protected AuNPs) and investigated the effect of surface chemistry on the self-assembly of AuNPs to achieve excellent evaporation efficiency using photoexcited plasma heating.[40] However, the high cost, scarcity and complex preparation process of gold nanomaterials limit their practical applications.

Carbon-based photothermal materials, especially carbon nanotubes, graphene and carbon black, are characterized by

[a]College of Textile and Apparel, Xinjiang University, Urumqi 830000, Xinjiang, China
[b]Institute of Smart & Ecological Textile, Quanzhou Normal University, Fujian 362002, China
[c]College of Textiles and Apparel, Quanzhou Normal University, Fujian 362002, China. E-mail: qhqh123@126.com

† Electronic supplementary information (ESI) available. See DOI: https://doi.org/10.1039/d4ra05241b

a wide range of light absorption and good chemical stability. These materials have been increasingly utilized in the field of photothermal conversion. For instance, Li *et al.* reported on carbon nanotubes as an efficient solar team generator. The composite evaporator, prepared by embedding multi-armed carbon nanotubes (CNTs) and polydopamine (PDA) on an ES nonwoven fabric, exhibits excellent light absorption and hydrophilicity. Under 1.0 solar irradiation. The light absorption rate reaches as high as 90.77%, and the water evaporation rate is 1.29 kg m^{-2} h^{-1}.[41] However, carbon-based photothermal materials have limitations in terms of thermal conductivity. Semiconductor photothermal materials are receiving increasing attention in the field of solar vapour dialysis due to their low cost, high photothermal conversion efficiency, excellent photostability, and enhanced near-infrared (NIR) absorption through excitation of local surface plasmon resonances (LSPRs). Hang *et al.* reported an extremely simple and low-cost interfacial heating film for high-efficiency solar steam generation. The composite film consists of a viscose cellulose film loaded with CuS hollow nanospheres. The CuS/cellulose composite film, prepared using a solvothermal method, functions as a highly efficient solar absorber (>94.0%), vapor channel, and thermal insulator (with a thermal conductivity of 0.06 W m^{-1} K^{-1}), achieving an efficiency of 85% under solar irradiation (1.0 kW m^{-2}).[42] During seawater evaporation, salt crystals continue to accumulate on the surface of composites, significantly reducing the efficiency of the evaporation process. The hydrophobic treatment of the surface by chemical reagents can well prevent the generation of salt crystals. Zhang *et al.* reported the preparation of a hydrophobic and porous carbon nanofiber (HPCNF) by combining porogen sublimation and fluorination. Under sunlight irradiation, the evaporation rate and efficiency can reach up to 1.43 kg m^{-2} h^{-1} and 87.5%, respectively.[43] Importantly, the exceptional water resistance provides the absorber with superior corrosion resistance and salt rejection performance. Surface fluoridation is likely to cause environmental pollution and even secondary pollution of water due to incorrect preparation and application methods. Therefore, it is particularly important to develop more environmentally friendly methods to resist salt crystallisation.

Fibrous materials with unique flexibility, durability, processability, practicability, and multifunctionality have attracted considerable attention in the ISSG field. Ge *et al.* reported the basics of fibrous materials, such as their classification, manufacturing methods and flexible fibrous structure, are firstly introduced. The outstanding properties of fibrous materials on different dimensions are demonstrated, as well as the versatile morphologies and structures that allow fibrous materials to carry out different roles in ISSG.[44] Nonwoven materials are also gradually being used for interface evaporation due to their low production costs and other characteristics. Zhao *et al.* This article reviews the recent progress of electrospun nanofiber-based evaporation systems focusing on polymer selection, available solar materials, incorporation strategies of solar materials, system configurations, factors influencing the performance, and applications of electrospun nanofiber evaporation systems.[45] Chong *et al.* hydrophobic industrial-grade carbon fiber membrane (CFM) with good photoabsorption was surface-modified with polydopamine (PDA) to prepare superhydrophilic CFM@PDA for the construction of efficient hanging-model evaporators without salt accumulation.[46] Needle-punched PET nonwoven materials are made of PET fibres, which have the characteristics of cost-effective, high porosity, fluffy and soft. Therefore, the fabrication of durable nonwoven fabric-based evaporators has considerable potential for application.

Herein, inspired by nature, we have designed interfacial evaporators with lotus leaf-like vertical water-conducting structures, which effectively utilize concentration differences to drive reduced salt crystallization and can be used for sustained solar-powered evaporation and desalination. We fabricated 2D/3D micro- and nanostructured graphene nanosheets/copper sulphide nanowires with a synergistic photothermal effect by coating graphene nanosheets on needle-punched nonwoven fabrics using a spraying method. Subsequently, biphasic copper sulphide $Cu_{2-x}S$ ($0 < x < 1$) was generated through *in situ* oxidation and precipitation transformations. The hierarchical structure of GO/Cu_xS @PET composites promotes light reflection and scattering, while the combined photothermal effect of GO and Cu_xS significantly improves light absorption. On this basis, the mechanisms of resistance to evaporation and salt crystallization of the composites were proposed. The excellent evaporation stability of the prepared nonwoven composites makes them potential candidates for treating seawater and wastewater.

2 Materials and methods

2.1 Materials

Needle-punched polyester nonwoven fabric (110 g m^{-2}) was provided by Zhuofang Industry Co., Ltd, (Dongguan, China). Graphene oxide (length $\leq$ 30.0 μm, diameter 15 $\pm$ 5.0 nm) was purchased from Shanghai Aladdin Reagent Co., Ltd, (Shanghai, China). Polyvinyl alcohol pellets, copper chloride dihydrate ($CuCl_2 \cdot 2H_2O$), sodium hydroxide (NaOH) and sodium sulphate (Na_2S), and anhydrous ethanol were purchased from McLean Reagent Co., Ltd, (Shanghai, China). All chemicals were used without further purification.

2.2 Fabrication of the composite evaporator

2.2.1 Fabrication of PVA@PET. Needle-punched polyester nonwoven fabric was used as a prototype (PET), and 2.0 g of PVA was dissolved in 100 ml of deionized water and stirred at 90 °C for 2 hours to obtain an aqueous solution of polyvinyl alcohol. PVA-PET (PPET) was obtained by spraying onto the PET surface using a spray gun. Subsequently, the obtained CES was divided into several nonwoven fabrics with an area of 9.0 cm^2 for further experiments.

2.2.2 Fabrication of GO@PET. Surface impurities were removed by sequentially ultrasonically cleaning virgin needle-punched polyester nonwoven (PET) fabric (90 mm × 90 mm) in ethanol and deionized water. GO (5.0 mg) was dispersed in an anhydrous ethanol solution at a concentration of 5.0 g L^{-1} and ultrasonicated for 30 minutes. The graphene oxide (GO)

solution was then sprayed onto the pretreated needle-punched nonwovens using a spray gun. The samples were dried at 60 °C for 30 minutes to obtain GO-PET. PVA (2.0 g) was dissolved in 100 ml of deionized water and stirred at 90 °C for 2 hours to obtain an aqueous polyvinyl alcohol solution. PVA-GO-PET (GPET) was obtained by spraying onto GO-PET using a spray gun.

2.2.3 Fabrication of Cu_xS@PET and Cu_xS@ PVA-GO-PET. Alkali-assisted oxidation and sulfidation were utilized to achieve *in situ* growth of copper sulphide on the fibers. Firstly, the needle-punched polyester nonwoven fabric was immersed in a 0.2 mol per L $CuCl_2$ solution. It was then immersed in a 0.5 mol per L NaOH solution for 5 seconds and finally submerged in a 7.0 mmol per L Na_2S solution for 30 minutes. After each step, the tissue was thoroughly rinsed with deionized water and then dried in an oven at 60 °C for 4 hours to obtain Cu_xS@PET (SPET). Using PVA-GO-PET sample as the substrate, Cu_xS@PVA-GO-PET can be obtained through the aforementioned preparation process.

2.3 Characterization

Scanning electron microscopy (SEM, TESCAN MIRA LMS, Czech Republic) was used to characterize the micromorphology and elemental distribution of the solar interface composite evaporator. The surface chemistry of the coated PET fibres was analysed by FTIR spectrometer (ATR, Thermo Scientific Nicolet iN10, USA), X-ray diffractometer (Rigaku SmartLab SE, Japan), and X-ray photoelectron spectrometer (Thermo Scientific K-Alpha, USA). The ultraviolet-visible-near-infrared absorption spectrometer (Shimadzu UV-3600i Plus, Japan) was used to determine the light absorption capacity of the evaporator in the wavelength range of 200 to 2500 nm. A sunlight simulator (Sola-500 T Nbet, Beijing, China) and a handheld infrared thermal imager (FLIR-E64501, US) was used in combination to evaluate the photothermal conversion efficiency of the evaporator. The surface wettability of the composite was characterized by measuring the water contact angle using an optical contact angle meter (CA-100A Innuo, Shanghai, China). An inductively coupled plasma spectrometer (Optima 7300 DV, USA) was used to measure the ion concentration of the simulated seawater before and after the solar desalination process. Carrier concentration, resistivity and mobility were measured using Hall Effect Tester (Ecopia HMS-7000, Korea). The wettability of the composite surfaces was characterized using an optical contact angle meter (CA-100A Innuo, Shanghai, China).

2.4 Solar-driven evaporation measurement

Experimental data were obtained from a solar evaporator operating within a temperature range of 25.0 ± 1.0 °C and 60.0–70.0% humidity. Analogously, a sunlight source (Sola-500 T Nbet, Beijing, China) was used to provide various sunlight intensities for radiation, while an infrared thermal image was captured using an infrared thermal camera (FLIR-E64501, USA). An optical power meter (FZ400, Nbet, Beijing, China) was used to test the power of simulated sunlight. The temperature of the sample surface and water was recorded using a multi-channel thermocouple temperature tester (TA612C, TASi, China). An electronic balance (FA224C, Bona, China) was used to record changes in water mass during evaporation. Freshwater was collected in a lidded cylindrical acrylic container for evaporation experiments.

3 Results and discussion

3.1 Preparation of the photothermal layer

The preparation process of the composite evaporator Cu_xS@PVA-GO-PET photothermal layer is depicted in Fig. 1a, where

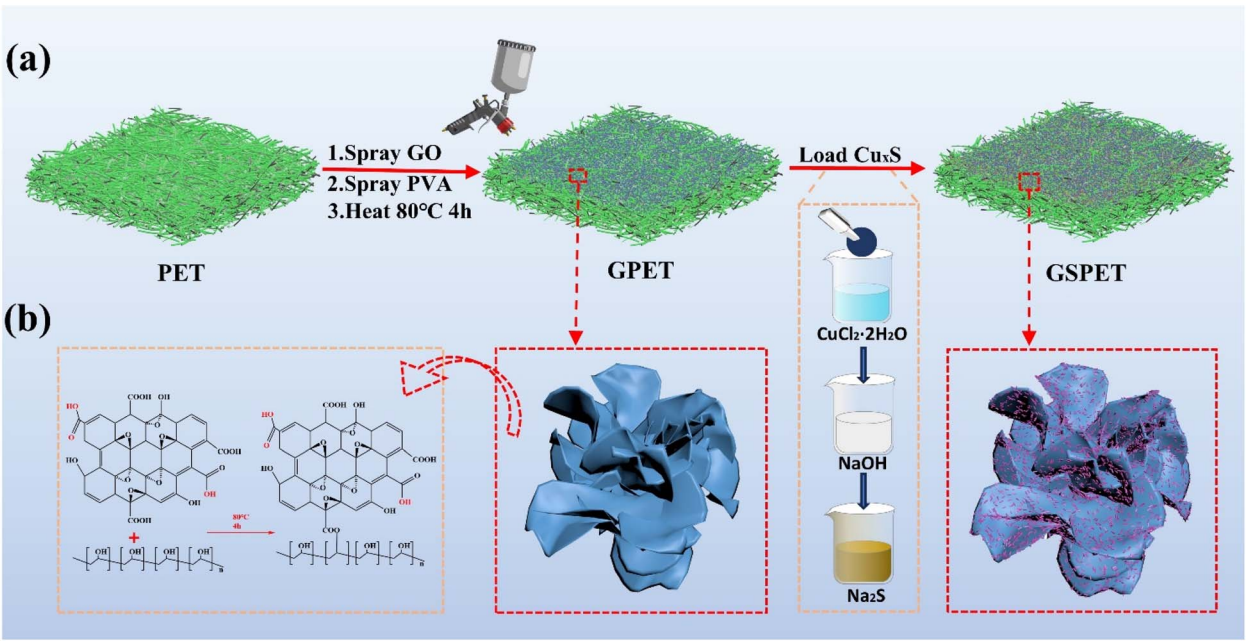

Fig. 1 (a) Schemes for the preparation of GSPET, and microcharacterization of photothermal materials. (b) Process of cross-linking GO and PVA.

a commercial needle-punched PET nonwoven (110 g m^{-2}) was used as the substrate. In addition to the advantages of chemical resistance and low cost, the multi-fine porous structure of PET nonwovens provides effective core absorption, while the high porosity enhances interfacial evaporation performance. Graphene oxide (GO) was utilized as a heat-absorbing material, which was sprayed onto the upper surface of PET and then dried at 80 °C for 10 minutes. The PVA solution was then sprayed onto the surface to coat the GO particles. Cross-linking occurs between the –OH group of PVA and the –COOH on the graphene oxide sheet to form an ester bond at high temperature (100 °C)[47–49] Fig. 1b. And, the changes in chemical group content after cross-linking of PVA and GO can also be clearly seen by XPS test analysis Fig. S1,† and high-resolution XPS spectra of C 1s and O 1s XPS clearly shows that the cross-linking has a larger area and an increased number of ester groups. Fig. S2.† In addition, due to the connect of graphene oxide and PVA, more gaps are formed on the fiber surface, which increases the specific surface area of the fiber. The original non-woven material consists of PET fibers with fewer reactive groups except for the two end hydroxyl groups of the molecular chain. The introduction of PVA makes the fibers have a large number of reactive groups, which can adsorb copper ions onto the surface of the PVA film through van der Waals forces (intermolecular forces). So that copper ions form a physical adsorption layer of monomolecular multimolecular layers on the membrane surface. It greatly increases the loading of Cu_xS, which is favourable to the photothermal effect. The Cu^{2+}-coated fabrics were subsequently immersed in NaOH solution and grew into dense and robust $Cu(OH)_2$ nanostructures on the fiber surface. Since the solubility product constant (K_{sp}) of Cu_2S (2.5×10^{-48}) is much smaller than that of $Cu(OH)_2$ (2.2×10^{-20}).[24,50] A precipitation transformation process was used to immerse the $Cu(OH)_2$ samples directly into Na_2S aqueous solution to obtain dense and robust Cu_2S nanoparticles.

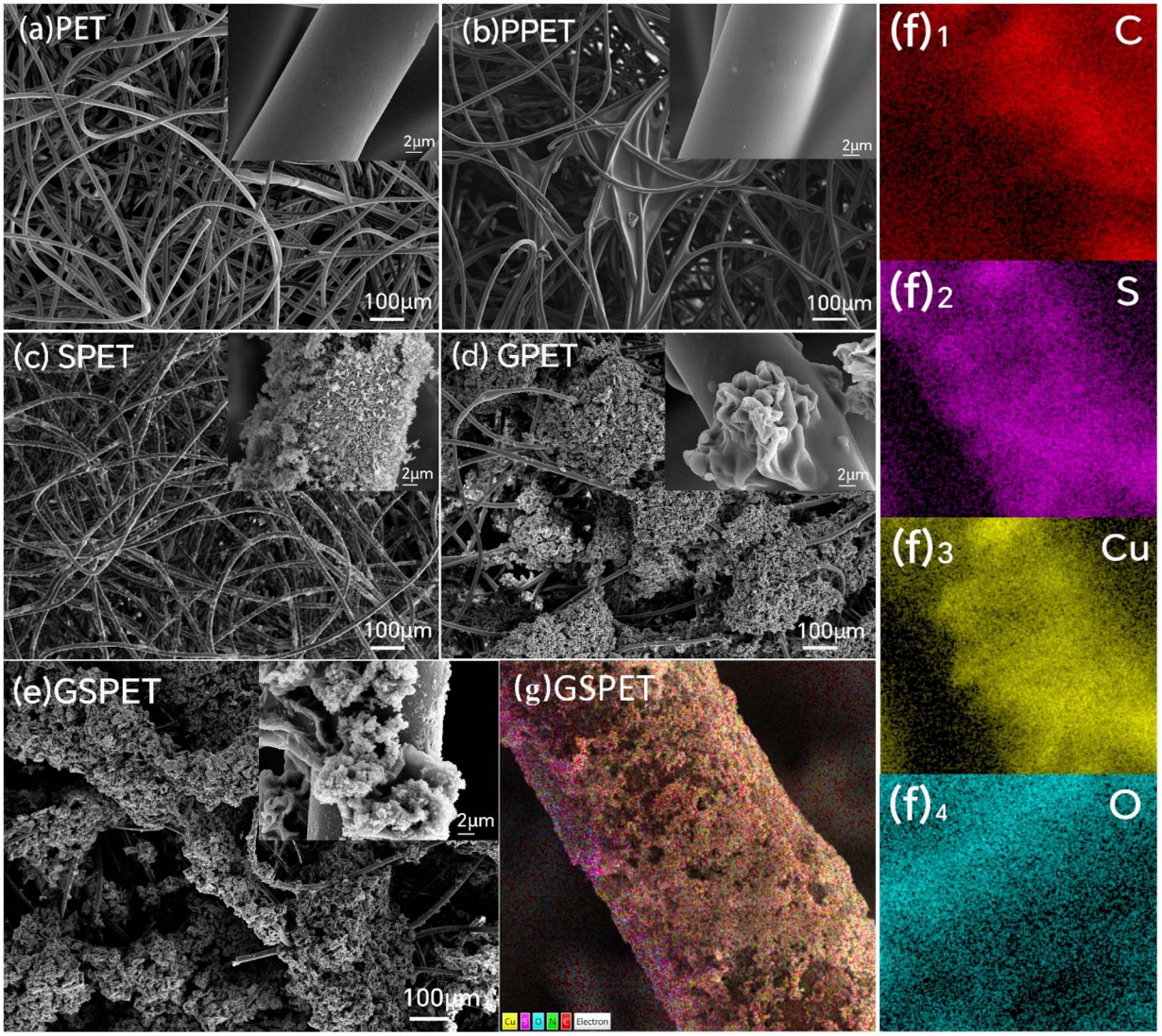

Fig. 2 SEM images of (a) PET, (b) PPET (PVA@PET), (c) SPET (Cu_xS@PET), (d) GPET (GO@PET), and (e) GSPET (CuxS/GO@ES) surfaces at different magnifications. Elemental distributions (f(1))–(f(4)) and elemental content analysis plots (g) of GSPET.

3.2 Characterization of the composites

Field emission scanning electron microscopy (SEM) was used to obtain micromorphological and optical images of PET, GPET, SPET and GSPET. The surface of the raw PET fibers was smooth (Fig. 2a). The microscopic morphology of GPET after spraying shows that the fiber surface is overed with numerous graphene oxide particles coated with polyvinyl alcohol, creating a rough cluster structure (Fig. 2b). Additionally, more voids are formed on the surface, increasing the specific surface area of the fiber. This promotes diffuse reflection of light, increasing the efficiency of photothermal conversion. In addition, the dense copper sulphide nanoparticles grown *in situ* on the surface of PET fibers, forming a hierarchical structure, could be observed through the microscopic morphology of the SPET. The fibers were covered with massive copper sulphide particles exhibiting a wavy nanoscale structure (Fig. 2c). The presence of poly (vinyl alcohol) introduced a large number of hydroxyl groups, enabling the growth of nanoscale copper sulphide in large quantities on the surface (Fig. 2d). This increased the loading of Cu_2S and led to a rougher surface for the flower-clustered graphene fibers. Formation of micrometer/nanometer-scale structures composed of GO and Cu_2S particles. The gradient porous micro/nanostructure with a rough surface increases the specific surface area of the fiber. This structure also reduces the specular reflection of light and enhances the light absorption on the fiber surface, thereby increasing the photothermal conversion efficiency.

The elemental composition of GSPET is illustrated in Fig. 2e. Fig. 2f(1)–f(3) illustrate the uniform distribution of the target elements C, Cu, and S. The elemental contents and distributions of the different samples are further compared in Fig. S1.† Only elements C, N and O are present on the surface of PET and GPET, while elements S and Cu are present in SPET and GSPET. These differences are attributed to the treatment with $CuCl_2$, NaOH, and Na_2S solution, which resulted in an abundance of copper sulphide on the surface of SPET and GSPET. The elements C, N, O, Cu and S were uniformly distributed across the entire surface of the modified PET, confirming the homogeneity of the *in situ* growth.

Fourier Transform Infrared (FTIR) characterization revealed changes in the chemical groups of PET, PPET, GPET, SPET and GSPET, displaying characteristic peaks of –OH and ethyl after PVA loading (Fig. 3a). These peaks were still clearly visible after the *in situ* loading of GO and Cu_xS. The characteristic PET peaks at 1408 cm^{-1} and 1339 cm^{-1} were obscured, resulting in a decrease in the peaks, which indicates the successful loading of these two substances. The results show that graphite oxide has a broader and stronger absorption peak at 3430 cm^{-1}, which is attributed to the stretching vibrational peak of –OH groups. The telescopic vibrational peak of C=O on the carbonyl group of graphite oxide is observed at 1725 cm^{-1}. The absorption peak at 1630 cm^{-1} corresponds to the bending vibrational absorption peak of C–OH, while the peak at 1110 cm^{-1} represents the vibrational absorption peak of C–O–C. In the XRD test curve, a sharp diffraction peak at $2\theta = 12.9°$ was observed due to the (002) reflection of graphene oxide (Fig. 3b). Another sharp diffraction peak at $2\theta = 43.3°$ was attributed to the (101) reflection of graphene oxide, providing evidence of successful loading of GO.

The XRD curves at 2θ of 32.28° and 48.6° showed diffraction peaks corresponding to reflections from the (103) and (110) crystal planes, respectively. This observation could confirm the successful growth of copper sulphide. The SPET samples were analyzed to determine the type of copper sulphide (Fig. 3c). The regenerated diffraction peaks correspond well to pyrochlore Cu_2S (JCPDS No. 1), and the diffraction peak at $2\theta = 54.0°$ can be

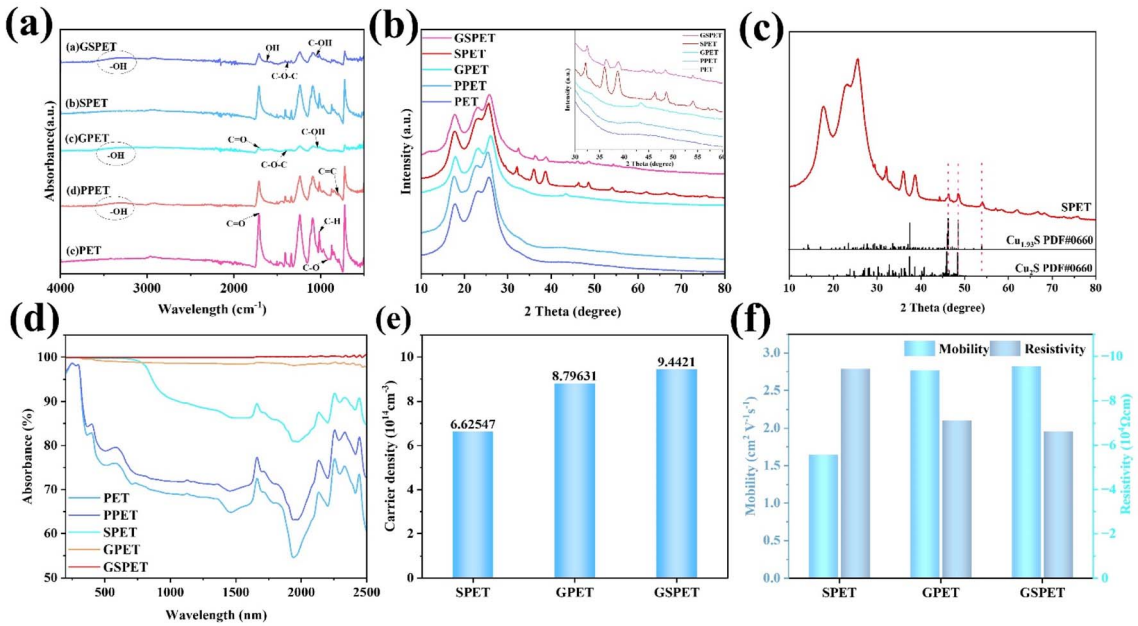

Fig. 3 (a) FTIR and (b) X-ray diffraction spectra of PET, PPET, GPET, SPET and GSPET. (c) XRD spectra of SPET with standard sample card. (d) Carrier concentration of SPET, SPET and GSPET. (e) Resistivity and mobility of SPET, SPET and GSPET. (f) Absorption spectra of PET, PPET, GPET, SPET and GSPET.

attributed to the presence of djurleite $Cu_{1.93}S$ (JCPDS No. 34-0660).[50] It should be noted that distinguishing between pyroxene and pear amphibole from X-ray diffraction (XRD) diagrams is challenging due to the similarity of their diffraction peaks. Therefore, xps tests were carried out to analyse the characteristic peaks of Cu 2p and S 2p, which were more pronounced (Fig. S1†). We further characterized the sample's carrier concentration, resistivity, mobility and UV-Vis-NIR spectra (Fig. 3d–f) to investigate the light absorption behaviour of the samples. Carrier concentration and mobility are the key factors affecting the photothermal effect. The carrier densities of SPET, GPET, and GSPET were 6.62547×10^{14}, 8.79631×10^{14}, and 9.4421×10^{14}, respectively. The high carrier densities favoured the enhancement of the LSPRs effect in the NIR region. The superior photothermal efficiency of GSPET was attributed to the compact stacking of chalcopyrite Cu_2S and syenite $Cu_{1.93}S$ in the Cu_xS composite in the Cu_xS composite, which synergistically enhances bandgap absorption and LSPRs throughout the solar spectrum. Overall, GSPET exhibits high carrier concentration and high mobility, which also contributes to its enhanced light absorption behaviour (Fig. 3f).

3.3 Evaporation performance

3.3.1 Wettability of the photothermal layer. Since the nonwoven substrate is produced through a needle-punching process, the pores on the surface and inside can absorb a large amount of water due to the core absorption effect. Inspired by the evapotranspiration of plant leaves, multiple water supply rods with vertical water supply are designed to facilitate rapid water supply for efficient evaporation from the interface. Optical and contact angle images of PET, GPET, SPET and GSPET were obtained using a contact angle meter and a camera (Fig. S3†). The results showed that the core absorption effect of the original PET nonwovens was superior. Even after loading graphene oxide and *in situ* growing copper sulphide, the core absorption effect on water was maintained, ensuring the final evaporation performance.

3.3.2 Solar evaporator preparation and photothermal performance. The solar evaporation performance of composites was investigated using a custom-designed hierarchical branch-structured solar-powered evaporation apparatus, which included a solar simulator, an interfacial evaporator, a seawater vessel, and an electronic balance (refer to Fig. 4a). The interfacial evaporator consists of a photothermal layer that acts as a solar absorber, EVA foam, hydroentangled cotton fabric to separate the photothermal layer from the EVA foam, and a waste humidifier pad (WHF) that functions as a water conveyor. In this system, the water transport capability of the WHF water guide pump is also crucial for achieving excellent evaporation rates. The water-guiding pump can elevate the dye solution up to 5.0 cm above the water within 10 seconds through the

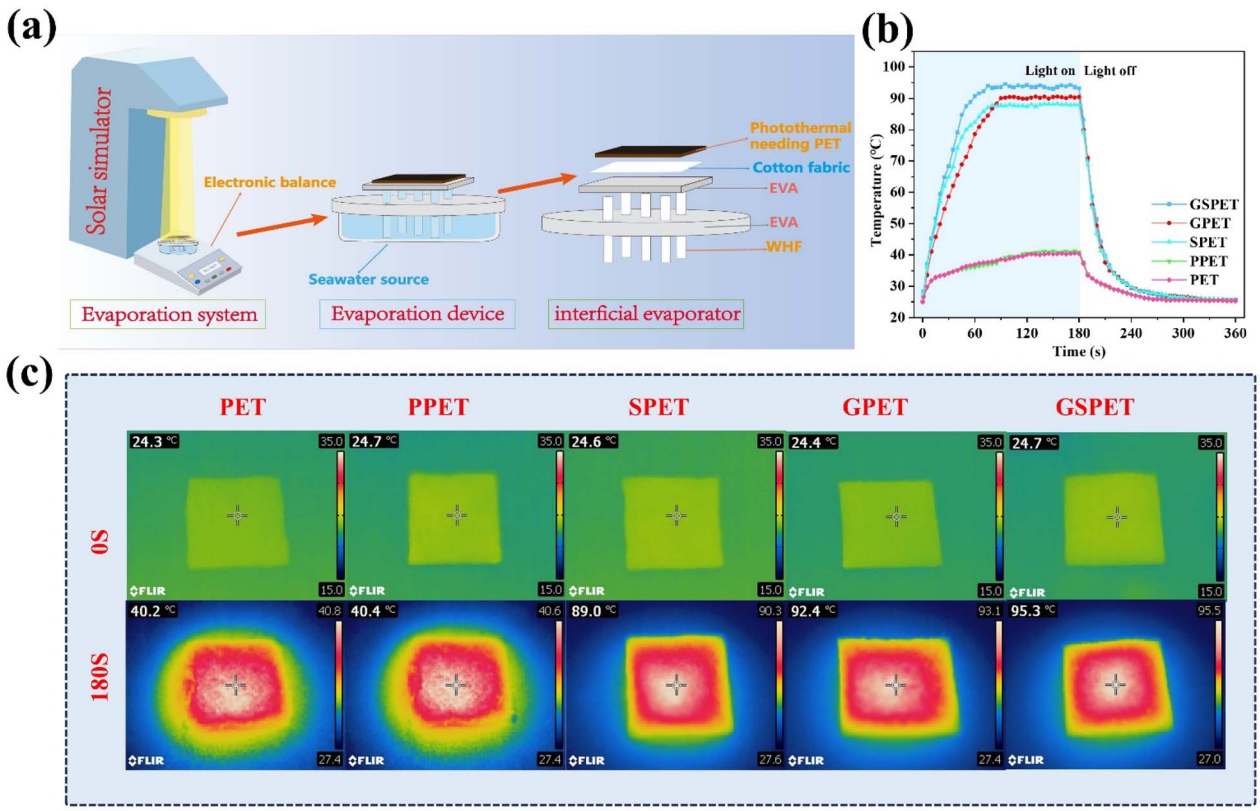

Fig. 4 Experimental setup for solar-powered interfacial evaporation. (b) The temperature rise and fall of dry PET, PPET, GPET, SPET and GSPET samples under one sun solar illumination. (c) Infrared images of PET, PPET, GPET, SPET and GSPET surfaces at the initial sate and equilibrium state after 180 s irradiation.

capillary action effect (Fig. S4†), demonstrating its high water-guiding capability. The hydroentangled cotton at the bottom of the photothermal layer ensured a uniform water supply. EVA foam was utilized to provide adequate support for the photothermal layer, enabling it to float and minimizing heat loss from the photothermal layer.

Photothermal conversion efficiency of different samples in dry conditions (Fig. 4b) was as follows: GSPET (93.6 °C) > GPET (90.6 °C) > GSPET (88.2 °C) > PPET (40.4 °C) = PET (40.5 °C). Before exposure to sunlight, the surface temperature of GSPET is approximately 24.5 °C, which is the same as room temperature. During an exposure period of 1.0 sun lux, the temperature significantly rises to 90.0 °C within 60 seconds and eventually stabilizes at 93.6 °C within 180 s (Fig. 4c). It is higher than that of GPET and SPET. This phenomenon is consistent with the results of UV-Vis-NIR spectroscopy. It indicates that the higher the absorptivity, the higher the thermal conversion rate, and consequently, the higher the surface temperature. This also suggests that the assembled Cu_xS and GO (2d/3d) structural combination enhances light absorption, promotes non-radiative recombination and facilitates the release of thermal energy.[24,51–54]

The polyvinyl alcohol (PVA) solely functions as an adhesive and does not contribute to the photothermal conversion effect. This is evidenced by the heating rate and final temperature of the PVA. For this reason, the PPET samples will not be discussed in the following experiments. High evaporation efficiency is crucial for the performance of an evaporator. Therefore, solar evaporation was systematically evaluated to determine water evaporation rates by monitoring the GSPET evaporator foam in real-time under 100 mW cm^{-2} of solar radiation. The results of the wet heating rate for different samples align with the dry heating rate (Fig. 5a), and the infrared image of the wet heating process is depicted in Fig. S5.† Excluding the natural evaporation of water (0.156 kg m^{-2} h^{-1}), this test demonstrates that both GPET and SPET evaporators outperformed PET in terms of evaporation efficiency (Fig. 5b), which is attributed to the excellent photothermal conversion of GO and Cu_xS. In particular, the GSPET evaporator loaded with both GO and Cu_xS exhibited the best evaporation efficiency (Fig. 5c). The order of magnitude of the evaporation efficiencies was as follows: GSPET (1.5079 kg m^{-2} h^{-1}) > GPET (1.3494 kg m^{-2} h^{-1}) > SPET (1.3178 kg m^{-2} h^{-1}) > PET (0.6721 kg m^{-2} h^{-1}).

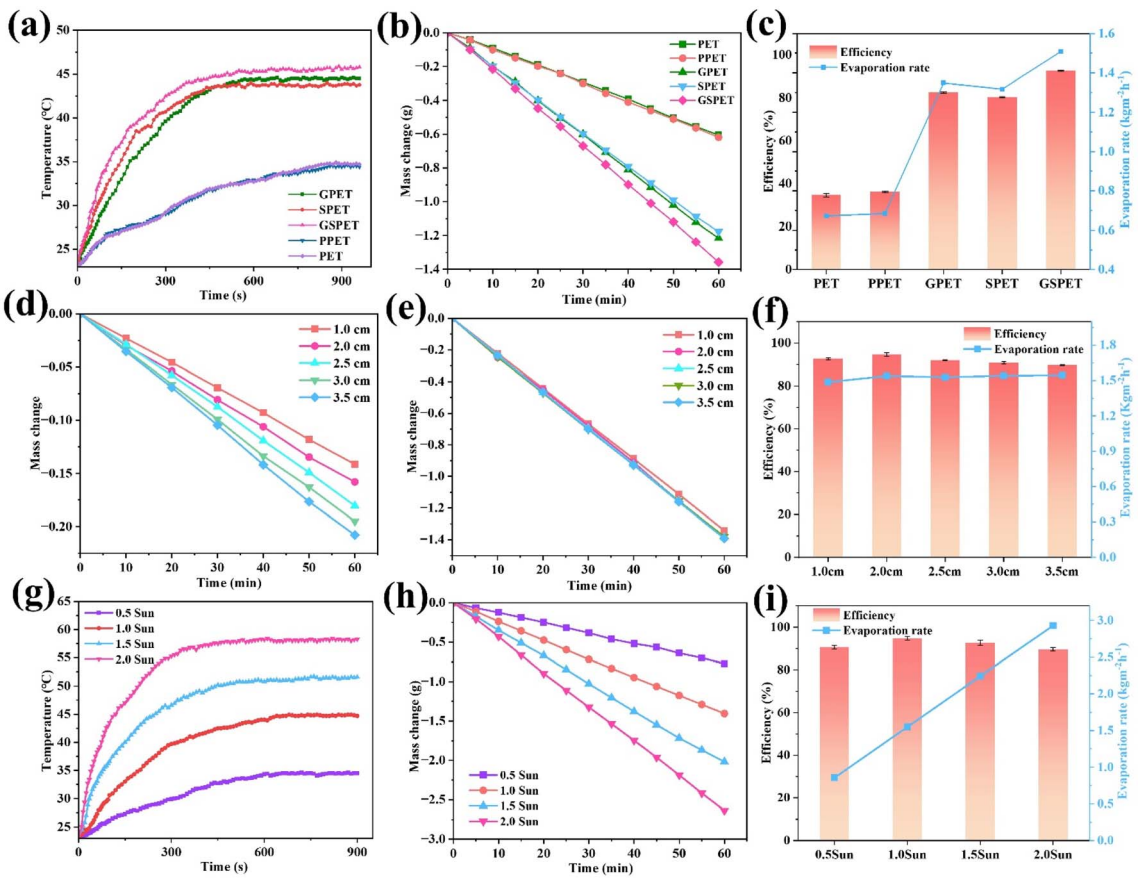

Fig. 5 (a) Temperature change of wet PET, PPET, GPET, SPET and GSPET samples under 1 sun light intensities. (b) Mass change of water under 1-sun irradiation and corresponding (c) evaporation rates and energy solar-to-vapor efficiencies. (d) Mass change of GSPET evaporator in dark environment at 1.0, 1.5, 2.0, 2.5, 3.0 and 3.5 cm water supply heights. (e) Mass change of water under 1.0-sun irradiation at different water supply heights and corresponding (f) evaporation rates and energy solar-to-vapor efficiencies. (g) Temperature variation of GSPET evaporator at 0.5 sun, 1.0 sun, 1.5 sun and 2.0 sun light intensities. (h) Mass changes of water under different illumination intensities. (i) Evaporation rates and energy solar-to-vapor efficiencies under different irradiation intensities.

To evaluate the solar steam evaporation capacity, the solar vapour conversion efficiency is calculated by the following equation[55]

$$\eta = \frac{mh_{lv}}{P_0 C_{opt}} \quad (1)$$

where m is the mass flux, h_{lv} is the total enthalpy of change of liquid vapour, including sensible and latent heat ($h_{lv} = C(T - T_0) + \Delta h_{vap}$), C_{opt} is the light concentration, and P_0 is the solar irradiation at a power density of 1 kW m^{-2}.

$$M = m_{solar} - m_{dark} \quad (2)$$

where m_{solar} is the evaporation rate under solar irradiation and m_{dark} (0.11 kg m^{-2} h^{-1}) is the evaporation rate under dark conditions.[56] As mentioned earlier, h_{Lv} consists of two components: sensible heat and enthalpy of phase change.[57]

3.3.3 Photothermal principle of solar evaporator. As mentioned above, the dry state temperature of sample GPET is higher than that of SPET. This is mainly due to the broader light absorption range of graphene oxide and the higher loading. Specifically, graphene oxide exhibits a higher carrier density and mobility than copper sulphide, as well as lower resistivity (Fig. 3d and e). When light irradiates the surface, two heat generation mechanisms come into play: non-radiative processes and thermal excitation. In the non-radiative composite, a pair of electrons and holes can move through the composite and transfer energy to another carrier. This process increases the kinetic energy of specific carriers, making it easier for them to overcome the potential barrier and transition back from the conduction band to the valence band. As a result, the heat generation rate of the sample increases, enhancing the effect of photothermal conversion.[58,59] It also triggers the thermal excitation mechanism, where light energy is absorbed and directly converted into thermal excitation of electrons and lattice. This process releases a significant amount of thermal energy, resulting in a further increase in the temperature of the entire composite. Under the same light conditions, copper sulphide heats up at a faster rate than graphene oxide. This equilibrium is attributed to the interaction between band gap absorption and the localized surface plasmon resonances (LSPRs) in the Cu_xS composites, as well as the properties of three-dimensional metal compounds. The formation of the $Cu_{1.93}S$ phase results in Cu_xS composites with high carrier density and high resistivity. These composites effectively combine bandgap absorption and LSPRs to yield excellent optical characteristics across the solar spectrum. It has been reported that fully stoichiometric Cu_2S has a narrow band gap of 1.2 eV with no LSPRs, while copper with a high number of Cu vacancies exhibits strong LSPRs. The LSPRs of free carriers in $Cu_{2-x}S$ ($0 < x < 1$) semiconductors result in broad optical absorption in the UV-visible region (200–700 nm), a wider absorption edge around 660 nm, and significant light absorption in the NIR region (>700 nm). Significant LSPRs absorption is observed in the near-infrared region of the absorption spectrum, indicating the formation of the $Cu_{1.93}S$ phase, but with a wide band gap of 2.0 eV.[60] Therefore, it is challenging to balance the bandgap absorption and LSPRs of single-phase $Cu_{2-x}S$ ($0 < x < 1$) across the entire spectral range of 250 nm to 2500 nm. The XRD analysis demonstrates the generation of two-phase Cu_xS composites (Cu_2S and $Cu_{1.93}S$), effectively combining bandgap absorption and LSPRs. This combination results in excellent optical properties across the entire solar spectrum. In addition, according to the basic principles of semiconductor physics, the temperature (T) carrier transport rate (μ) of a semiconductor is related to the resistivity (ρ) as follows[61]

$$\mu \propto \left[\exp\frac{h\omega}{2\Pi k_0 t} - 1\right] \quad (3)$$

$$\rho = \frac{1}{nq\mu_n + pq\mu_p} \quad (4)$$

For formula (3), ω, k_0 and h represent angular frequency, Boltzmann constant and Planck constant, respectively. Based on this formula, it can be inferred that the higher the temperature of T, the larger μ. In the formula (4), n, p, q, μ_n and μ_p are concentration of electrons, concentration of holes, charge quantity, charge transfer rate of n-type and p-type semiconductors, respectively.[62] It can be observed that as the temperature increases, the rate of photogenerated carrier transport also increases, while the resistance decreases. The high temperature of graphene oxide under light accelerates the carrier separation and photo-induced charge transfer of Cu_xS, reducing their compound and ultimately enhancing its thermal conductivity.[63–65] Copper sulphide is a three-dimensional metallic compound with excellent thermal conductivity, which facilitates the efficient transfer of internal heat to the surface of the composite. On the other hand, graphene oxide is a two-dimensional material that impedes the rapid transfer of internally generated heat to the material's surface.[66] Notably, the graphene oxide/copper sulphide (2D/3D) structure exhibits an outstanding light trapping effect. The synergistic photothermal effect of both materials enables the GSPET to achieve optimal light absorption, high carrier concentration, mobility, and low resistivity characteristics across the entire wavelength range (300–2500 nm). Consequently, it is distinguished by its high temperature and rapid temperature ris.[67,68]

3.3.4 Thermal management of evaporator. The physical model of the interface evaporator is shown in Fig. S6a.†A vertically aligned vessel-enhanced convection evaporator was designed to effectively reduce salt crystallization. The water guide bar is in direct contact with the water and supplies water to the photothermal layer of the evaporator. The heat generated by the absorption of sunlight by polystyrene is primarily concentrated on the surface of the non-woven material, while the downward heat transfer is restricted to the polystyrene foam. Heat loss calculations show (Notes S1†) that convective heat loss is 1.14%, radiative heat loss is 3.47%, and conductive heat loss is as high as 1.19% (Fig. S6b†). Taking advantage of the hierarchical branching structure and the synergistic enhancement of band gap absorption with LSPRs, GSPET achieves a high energy conversion efficiency of 94.71%. The

interface evaporation system has minimal thermal conductivity loss, which further elucidates the heat transfer mechanism of the evaporator. Detailed calculations are described in the ESI.†

3.3.5 Effect of light intensity and water supply on evaporative performance. To investigate the relationship between water supply and GSPET evaporation rate, evaporators with varying water supply heights ranging from 1.0 cm to 3.5 cm were set up to measure the mass changes of evaporation at different heights in both dark ambient conditions (Fig. 5d) and under 1.0-sun irradiation (Fig. 5e). When the evaporation test was conducted in the dark, the rate of evaporation was found to be proportional to the height of the water gauge bar (Fig. 5f). Evaporation rates of approximately 1.56 kg m^{-2} h^{-1} were achieved for both 2.0 cm and 3.5 cm water supply heights under 1.0-sun irradiation. However, the respective evaporation efficiencies were 94.71% and 89.74%. This was attributed to the fact that the water supply height affects the evaporation efficiency of water in a dark environment. When the water supply height exceeded 1.0 cm, the water supply time was prolonged, and the surface temperature of the photothermal layer increased with the increase in the height of the water guide rod (Fig. S7†). At 2.0 cm, the water evaporation rate was closest to the water supply rate and the evaporation rate was optimal. The water supply was too high at 3.5 cm, which made it impossible for the water to reach the top in time. Additionally, the evaporation rate did not increase despite the higher surface temperature. It is worth noting that under simulated sunlight, the light irradiation causes a slight increase in the temperature of the water guide rod near the end of the photothermal layer. This increase results in a disguised expansion of the effective evaporation area, which is beneficial for enhancing evaporation efficiency (Fig. S7†). Despite the photothermal layer's temperature being slightly higher than that of other evaporators at different heights, the evaporation efficiency did not increase. Evidence shows that there is an equilibrium between water supply and evaporation, and evaporation efficiency is highest when the two are balanced. In addition, a reliable water supply is essential for preventing salt deposition and achieving stable desalination performance, while also ensuring optimal evaporation efficiency. These aspects will be further explored in the following sections. Thus, further enhancing solar evaporation performance primarily involves expanding the evaporation area and effectively integrating water supply. Increasing evaporation rates for large-scale freshwater production requires higher solar radiation intensity. Therefore, it is critical to study how light intensity affects temperature in GSPET. An infrared camera was used to measure the surface temperature of GSPET under different light conditions ranging from 0.5 to 2.0 solar lux (Fig. 5g). The evaporation efficiency of the solar generators is characterized by the change in water mass under solar irradiation (Fig. 5h). The corresponding water evaporation rate and conversion efficiencies were calculated (Fig. 5i). The decrease in conversion efficiency can be attributed to higher photothermal temperatures, which lead to increased heat transfer, radiation and thermal convection losses. There is no significant reduction in evaporation efficiency due to the solar evaporator's efficient water transfer and thermal management capabilities. Due to the limited thermal conductivity of the EVA foam, a significant amount of heat accumulates in the top layer of the evaporator, which effectively hinders heat transfer to the water.

In addition to the aforementioned findings, the evaporation process of the composite solar evaporator is analyzed in Fig. 6. The layered structure created on the surface of GSPET fibers facilitates efficient light scattering.[56] This resulted in light not only being reflected within the micron-sized porous structure of the fabric but also undergoing multiple scattering due to the presence of GO and Cu_xS nanoparticles. As a result, light absorption is significantly enhanced. In addition, the

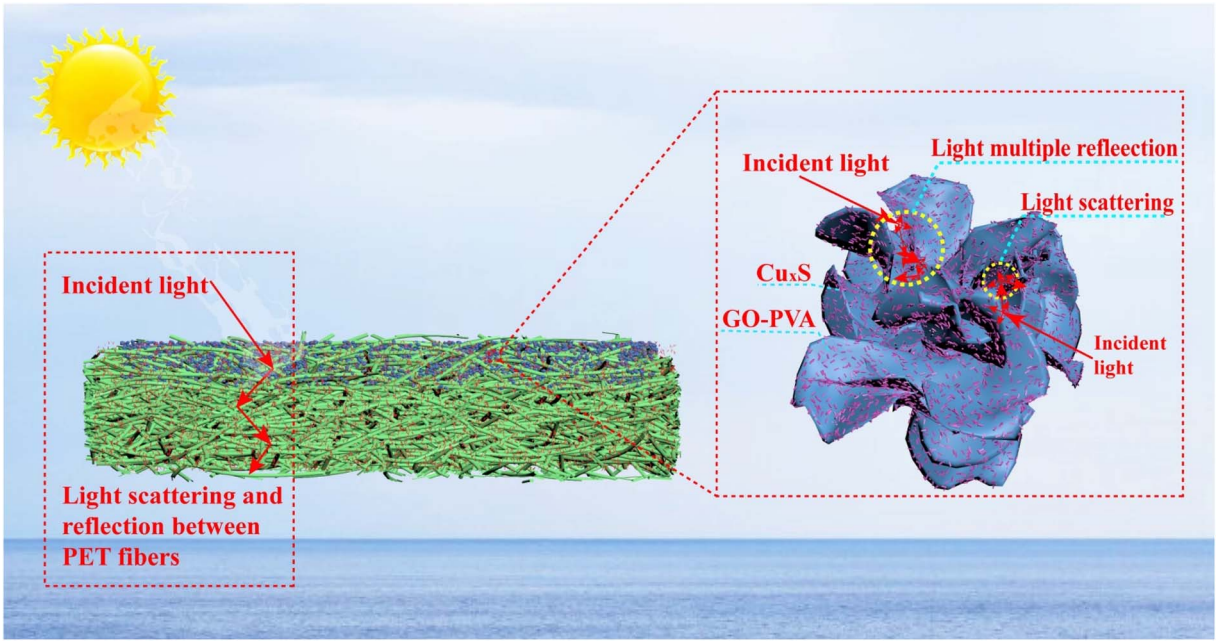

Fig. 6 Schematic of solar steam generation mechanism for the solar evaporator based on the GSPET.

synergistic effect of GO and Cu_xS can significantly enhance light absorption. With solar energy utilization. Our evaporation efficiency of 94.71% outperformed that of other solar interface evaporation composites (Table 1†).

3.4 Salt resistance and durability

The main components of seawater are inorganic salts, and their content changes with the geographical environment and seasonal ocean currents. In order to evaluate the application performance of GSPET samples under different salt concentration scenarios, the evaporation efficiency of GSPET was investigated under varying mass concentrations of NaCl solution and seawater (Fig. 7a and b). The results indicate that the evaporation efficiency of the photothermal evaporator decreases as the salt concentration increases from 0% to 20.0%. This is because the higher the brine salt concentration, the stronger the intermolecular forces that need to be overcome during the evaporation process. Furthermore, the increase in evaporation enthalpy results in a reduction in evaporation efficiency. To analyze the desalination performance of the GSPET evaporation system in real seawater, the vapors produced were collected using an acrylic tank, and then the ion concentrations were evaluated using ICP-OES. The concentrations of the four main ions (Ca^{2+}, K^+, Mg^{2+} and Na^+) before and after desalination are shown in Fig. 7c. It can be observed that the concentrations of the purified metal ions were all reduced by two to three orders of magnitude, significantly below the safe concentration levels set by the standards established by the World Health Organization (WHO).

Continuous operating efficiency and recirculation rate are also two key factors affecting the efficiency of desalination processes. During the 10 hours continuous seawater evaporation process in the GSPET evaporator, the evaporation rate slightly decreased due to the salt content in the seawater. However, the evaporation efficiency remained stable and efficient in the subsequent evaporation process (Fig. 7d). The GSPET evaporator was then tested on a ten-day cycle and found to maintain an evaporation efficiency of about 1.51 kg m^{-2} h^{-1} per unit of evaporation, which is approximately 92.31% (Fig. 7e). In addition, no salt crystals appeared on the surface

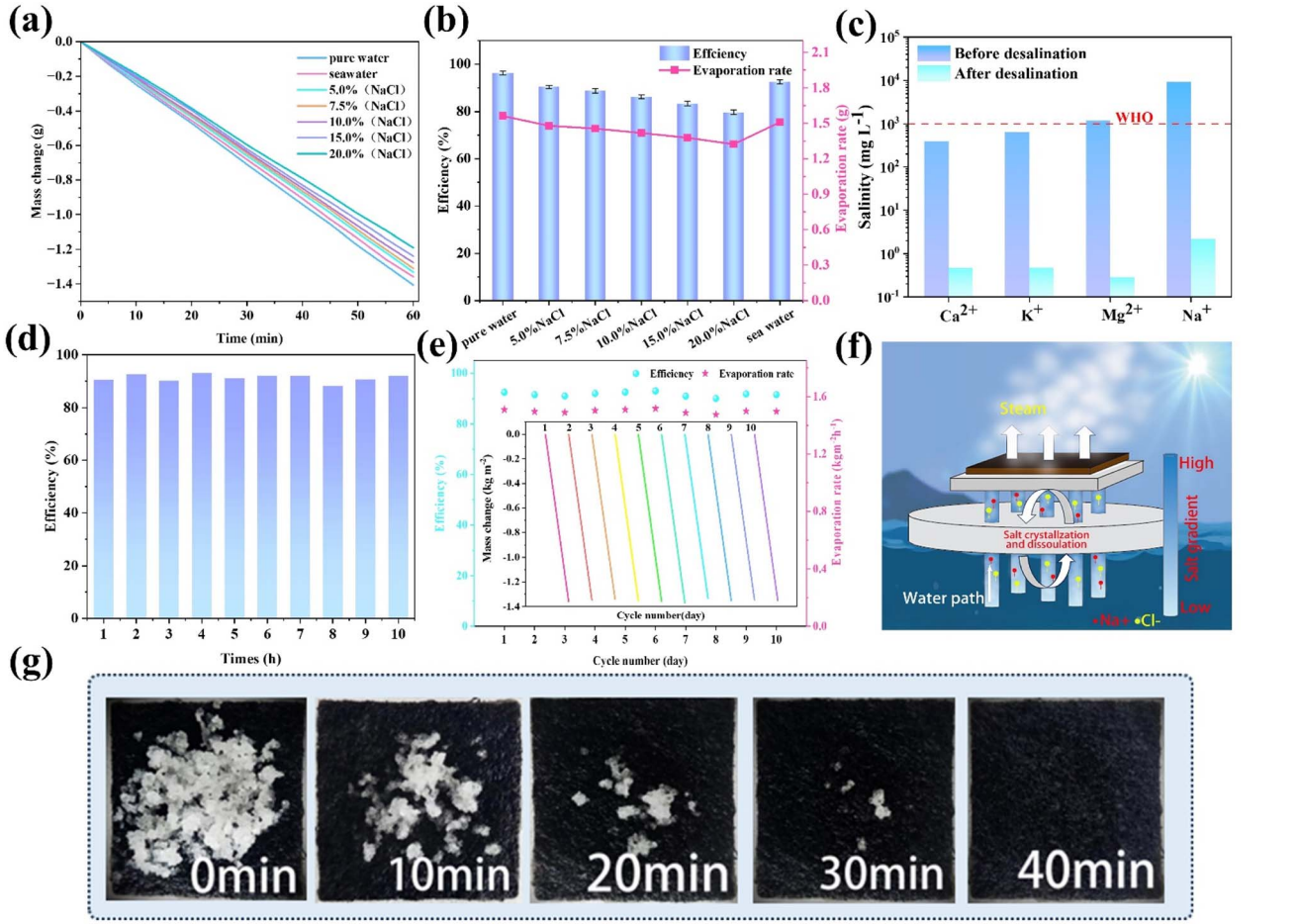

Fig. 7 (a) Mass changes, (b) efficiency of pure water, saline water (5.0, 7.5, 10.0, 15.0, 20.0 wt%) and seawater under 1.0 sun irradiation. (c) The ion concentrations of Na^+, Mg^{2+}, K^+, and Ca^{2+} of the seawater before and after desalination. (d) The variation of evaporation rates during the seawater desalination over a 10 hours period. (e) The variations of evaporation rates during 10 cycles when treating seawater. The inset pictures are the mass change of the GSPET during 10 cycles. (f) Schematic diagram of evaporator operation and salt resistance principle. (g) Digital pictures of a salt rejection progression of the GSPET under solar 1.0 sun irradiation.

after 4 hours of evaporation experiments with various salt concentrations and seawater (Fig. S8†). To assess the salt resistance of the GSPET evaporator, 1.0 g of NaCl crystals placed on the surface of the GSPET were completely dissolved after the solar evaporator was immersed in actual seawater for 40 min (Fig. 7g).

To investigate the salt suppression mechanism of the evaporator, experiments were conducted under simulated sunlight using simulated seawater as the water source. The phenomenon of NaCl flowing in the water source could be observed (Video S1†). Therefore, the salt suppression mechanism of the evaporator was summarized as diffusion and convection (Fig. 7f). Specifically, the photothermal and absorbent layers are moistened with simulated seawater before illumination, and the concentration of simulated seawater in the photothermal layer matches the concentration of water in the container. After turning on the light, the salt concentration in the photothermal layer quickly exceeds that of the water in the container due to evaporation. As a result, the evaporator can desalinate highly saline water through convection and diffusion. At the same time, enough simulated seawater is transferred from the vessel to the photothermal layer through the water guide rods. The high-salinity water in the photothermal layer is then transported back to the vessel, driven by the difference in chemical potentials between the two. This clearly demonstrates GSPET's salt tolerance and stability in seawater. The water washing experiments were performed on the GPET photothermal layer with and without a PVA coating (Video S2 and S3†).

After several shakes and oscillations in deionized water, the PVA-coated samples showed no residue remaining in the water after washing. In contrast, the GPET without PVA coating showed a significant amount of residue after washing (Fig. S9a and b†). Evaporation experiments were conducted on the GSPET samples after undergoing repeated water washing cycles. The evaporation rate remained constant at approximately 1.536 kg m^{-2} h^{-1}, with an evaporation efficiency of around 94.11%. These results suggest that the evaporator demonstrates excellent durability (Fig. 8a). This is mainly due to the strong adhesion resulting from the encapsulation of graphene oxide by PVA on the evaporator surface and the growth of copper sulphide on the PVA surface, forming strong chemical bonds. If the evaporator lacks a PVA coating, the photothermal material load might not be robust enough to resist being washed away by water. This could lead to a reduction in the photothermal efficiency of the evaporator.

3.5 Practical applications of solar evaporator

In order to confirm the excellent and sustainable purification performance of the GSPET evaporator for dyeing effluents, the effluent purification performance was assessed using simulated

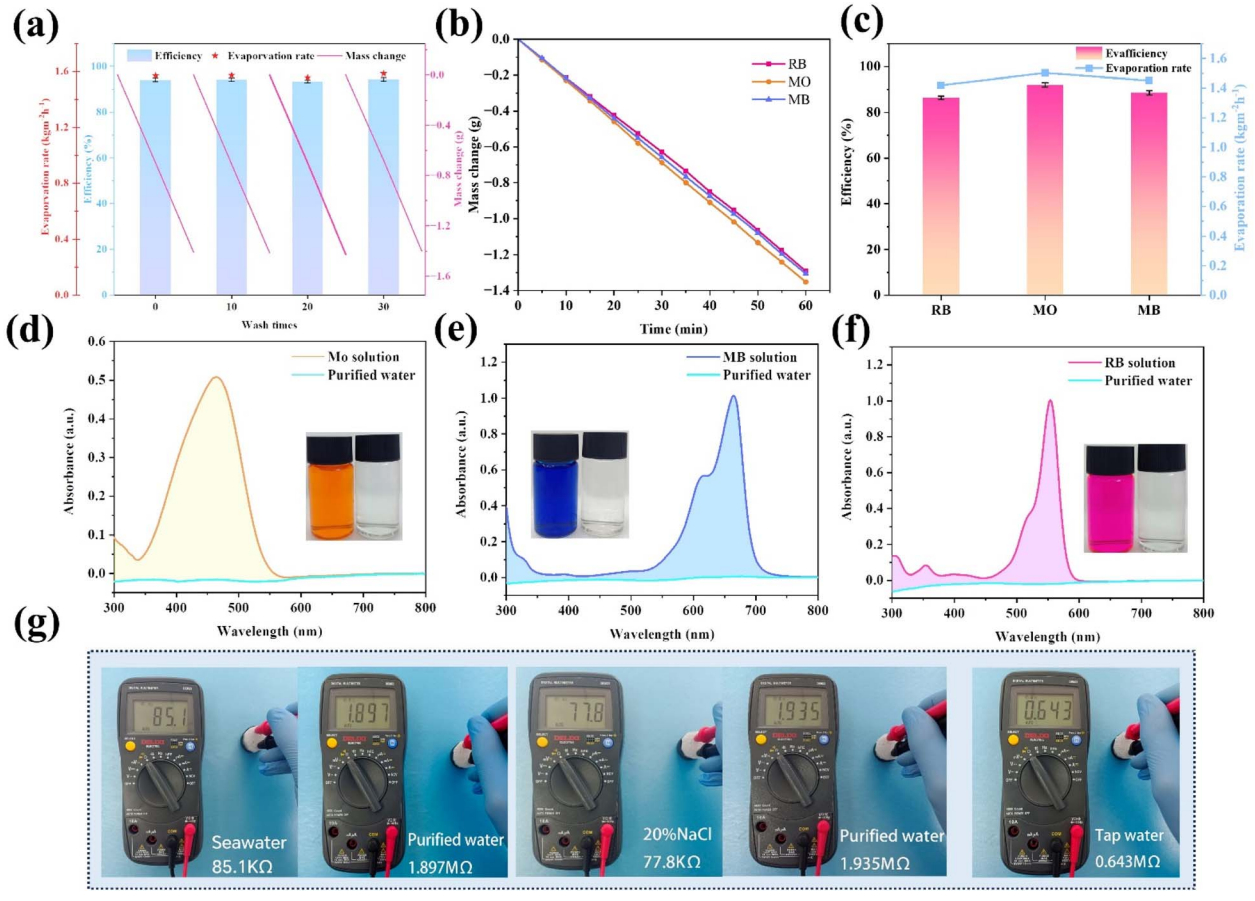

Fig. 8 (a) Mass change in, evaporation efficiency and evaporation rate after water washing, at one solar intensity. (b) Mass changes. (c) Efficiency and evaporation rate of RB, MO, MB water under 1.0 sun irradiation. (d)–(f) UV-vis spectra of dye wastewater before and after solar purification.

effluents containing methyl orange (MO), methylene blue (MB) and rhodamine B (RB) at concentrations of 10.0 mg L^{-1}. The evaporation efficiency of the solar generators is characterized by the change in water mass under solar irradiation (Fig. 8b), and the corresponding water evaporation rate is calculated (Fig. 8c). The evaporation rate was approximately 1.48 kg m^{-2} h^{-1}, which corresponds to an evaporation efficiency of around 90%. The orange, blue and red solutions became transparent after purification. In addition, the characteristic absorption peaks of methyl orange (465 nm), methylene blue (665 nm) and rhodamine B (554 nm) almost disappeared from the UV-visible spectrum of the treated wastewater. The concentration of residual dyes was negligible, confirming the complete removal of the dyes from the water (Fig. 8d–f). The resistance values of seawater samples and a 20.0% NaCl solution were tested before and after evaporation to assess water quality, further confirming the feasibility of GSPET in desalination applications. The resistance of the actual seawater was about 85.1 kΩ, while that of the distilled seawater was approximately 1.897 MΩ. There is a 22.3-fold increase in the resistance of the water purified by the GSPET evaporator. The resistance of the 20.0% NaCl solution was about 77.8 kΩ, while that of the distilled seawater was approximately 1.935 MΩ, indicating a significant decrease in the ionic concentration of the water (Fig. 8g). The electrical resistance of purified water is higher than that of tap water. This indicates that the quality of water after purification by GSPET evaporator is higher than that of domestic water, and the water quality is significantly improved. Evaporation under natural light is crucial for practical applications. An outdoor evaporation test was conducted using real seawater from the East China Sea to demonstrate its promising potential for practical application. Three sets of evaporation experimental setups, labelled A, B and C, were established to minimize experimental errors. Seawater was utilized as the water source for the evaporation experiments. All data were collected every 60 minutes from 9:00 a.m. to 5:00 pm during daylight hours. Light intensity, relative humidity, ambient temperature, and surface temperature were recorded (Fig. 9a). Due to the excellent light absorption capability of the photothermal layer, water vapor started to accumulate on the surface of the collector two hours after the experiment commenced (Fig. 9c). By 5:00 pm, more purified water had been collected in all three groups of evaporation experiments after 7 hours of exposure to natural light (Fig. 9d). Due to the influence of different breezes at various times, errors occurred in the experimental data. The average total mass change of the three groups of experiments was approximately 9.20 kg m^{-2}, which is sufficient to meet the water requirements of four individuals (Fig. 9b). The infrared photographs show that the temperature is lower than the box temperature due to the condensation of large amounts of water vapor at the top (Fig. 9e). Additionally, no salt crystals were observed on the evaporator surface at the end of the test. It is verified that the solar thermal conversion evaporator has efficient outdoor solar desalination capability and excellent potential for scalable practical applications.

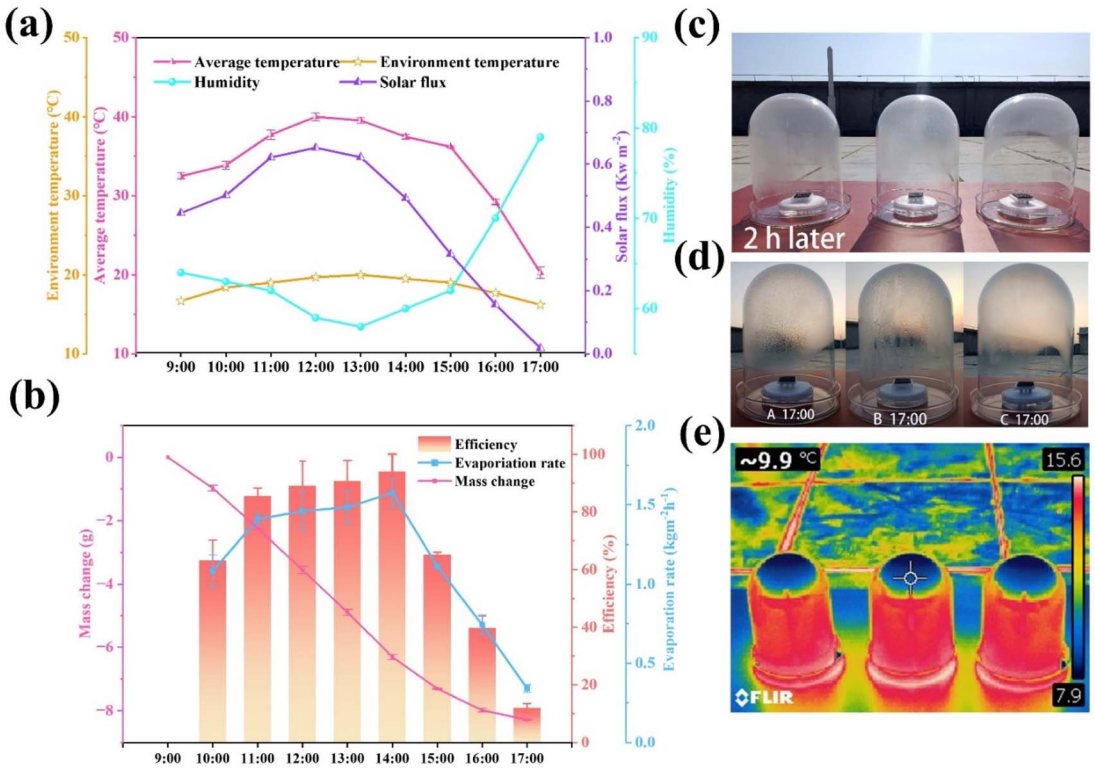

Fig. 9 (a) Variation of light intensity, relative humidity, ambient temperature, and surface temperature with the sun. (b) Mass changes, efficiency and evaporation rate of RB, MO, MB water under real light. (c) Photos of outdoor evaporation experimental device. (d) Collection of fresh water at the end of the experiment and (e) infrared photograph of the corresponding device.

Furthermore, the estimated cost of the developed photothermal evaporator is approximately $8.0712 per m^2 (Table S2†), the cost-effectiveness of the Cu_xS@ PVA-GO-PET is compared with that of the most recently reported evaporators, and it is found that the Cu_xS@PVA-GO-PET is highly cost-effective (Fig. S10†) Thus, the evaporator in this study not only demonstrates excellent evaporation efficiency, self-desalination capability, and sustained durability but also exhibits high cost-effectiveness. It is a candidate to become a practical material for desalination or freshwater production.

4 Conclusion

In this work, we coated graphene oxide (GO) *in situ* and grew Cu_xS on PET needle-punched nonwoven fabrics. We designed two-dimensional/three-dimensional microstructure graphene oxide nanosheets/copper sulphide nanowires (GO/Cu_xS) with synergistic photothermal effects. Additionally, a vertically aligned water-conducting rod structure was employed to enhance convection, thereby minimizing the formation of salt crystals. The strong adhesion and abundant active groups of PVA were utilized to ensure a high loading of photothermal materials. Under a single solar flux irradiation, the adhesion of GO resulted in a surface temperature reaching as high as 90.6 °C. The growth of Cu_xS further increased the surface temperature of the material to 93.6 °C without affecting the water absorption properties of the material. The combination of GO and Cu_xS coatings exhibited a synergistic effect, leading to an efficient photothermal performance on the evaporator surface. At a water supply height of 2.0 cm and solar irradiance of 1.0 kW m^{-2}, the evaporation rate was 1.5622 kg m^{-2} h^{-1} with a solar thermal efficiency of 94.61%. In addition, the concentration of salt ions in the fresh water evaporated by the GSPET composite was well below the drinking water standards set by the World Health Organization. More importantly, the GSPET evaporator maintained a high efficiency of 92.31% after 10 days of continuous use, ensuring long-term stable and reliable operation. Therefore, the GSPET evaporator has great potential for efficient and stable desalination under solar irradiation.

Data availability

The data are available from the corresponding author on reasonable request.

Author contributions

Wenbo Sun: investigation, data curation, writing – original draft. Huan Qi: conceptualization, methodology, writing – review & editing, formal analysis, supervision. Tan Li: software, validation. Minggang Lin: software, validation. Chuyang Zhang: project administration. Yiping Qiu: supervision. All the authors endorsed the final version of the manuscript.

Conflicts of interest

There are no conflicts to declare.

Acknowledgements

This research was funded by the Fujian Provincial Co-innovation Platform Project Program (No. 2021FX08). The authors are grateful to the Apparel of QNU for providing laboratory facilities.

Notes and references

1 Z. Liu, J. Ying, C. He, D. Guan, X. Pan, Y. Dai, B. Gong, K. He, C. Lv, X. Wang, J. Lin, Y. Liu and B. A. Bryan, *Landsc. Ecol.*, 2024, **39**, 86.
2 S. Greenhalgh and O. Samarasinghe, *Ecol. Soc.*, 2018, **23**, 44.
3 D. Zamrsky, G. H. P. Oude Essink and M. F. P. Bierkens, *Earth's Future*, 2024, **12**, e2023EF003581.
4 C. Chen, Y. Yang, C.-H. Lee, S. Takizawa, Z. Zhang, H. Y. Ng and L.-a. Hou, *Water Res.*, 2024, **253**, 121358.
5 L. B. Grossi, L. C. Lange and M. C. S. Amaral, *J. Cleaner Prod.*, 2024, **435**, 140521.
6 J. Kim, K. Park, D. R. Yang and S. Hong, *Appl. Energy*, 2019, **254**, 113733.
7 B. A. Shoemaker, O. Khalifa and A. Haji-Akbari, *ACS Nano*, 2024, **18**, 1420–1431.
8 Z. Zhu, J. Xu, Y. Liang, X. Luo, J. Chen, Z. Yang, J. He and Y. Chen, *Environ. Sci. Technol.*, 2024, **58**, 3800–3811.
9 X. Zhong, Y. Wu, P. Zhang, Y. Chen, Y. Cai, W. Wang, X. Min, J. Xiong and M. Li, *J. Cleaner Prod.*, 2023, **417**, 138827.
10 Z. Zheng, W. Li, H. Liu and X. Wang, *ACS Appl. Mater. Interfaces*, 2022, **14**, 50966–50981.
11 M. Yang, L. Zhang, D. Ye, Y. Dong, Y. Zhan and X. Jiang, *Chem. Eng. J.*, 2024, **480**, 148121.
12 W. Xie, P. Tang, Q. Wu, C. Chen, Z. Song, T. Li, Y. Bai, S. Lin, A. Tiraferri and B. Liu, *Chem. Eng. J.*, 2022, **428**, 132624.
13 R. Li, C. Zhou, L. Yang, J. Li, G. Zhang, J. Tian and W. Wu, *J. Hazard. Mater.*, 2022, **424**, 127559.
14 Y. Fan, W. Bai, P. Mu, Y. Su, Z. Zhu, H. Sun, W. Liang and A. Li, *Sol. Energy Mater. Sol. Cells*, 2020, **206**, 110268.
15 J. He, G. Zhao, P. Mu, H. Wei, Y. Su, H. Sun, Z. Zhu, W. Liang and A. Li, *Sol. Energy Mater. Sol. Cells*, 2019, **201**, 110141.
16 M. Xia, L. Chen, C. Zhang, Q.-M. Hasi, Z. Li and H. Li, *Appl. Clay Sci.*, 2020, **189**, 105519.
17 H. Ghasemi, G. Ni, A. M. Marconnet, J. Loomis, S. Yerci, N. Miljkovic and G. Chen, *Nat. Commun.*, 2014, **5**, 4449.
18 Q. Fang, T. Li, Z. Chen, H. Lin, P. Wang and F. Liu, *ACS Appl. Mater. Interfaces*, 2019, **11**, 10672–10679.
19 L. Zhang, B. Bai, N. Hu and H. Wang, *Sol. Energy Mater. Sol. Cells*, 2021, **221**, 110884.
20 J. Wu, X. Yang, X. Jia, J. Yang, X. Miao, D. Shao, H. Song and Y. Li, *Chem. Eng. J.*, 2023, **471**, 144365.
21 W. Chao, S. Pi, Y. Yang, Z. Li, Y. Yu, Y. Yang, R. Yang, H. Li and L. Lu, *Chem. Eng. J.*, 2023, **468**, 143593.
22 L. Sun, X. Zhang, H. Yuan, H. Cong, Y. Shi, J. Lu, W. Shi and F. Guo, *Chem. Eng. J.*, 2023, **477**, 147072.
23 J. Li, X. Zhou, G. Chen, F. Wang, J. Mao, Y. Long, H. Sun, Z. Zhu, W. Liang and A. Li, *Sol. Energy Mater. Sol. Cells*, 2021, **222**, 110965.

24 Z. Zhang, H. Liu, Z. Kong, M. Fang, M. Wang and Y. Zhu, *ACS Appl. Nano Mater.*, 2022, **5**, 4931–4937.
25 Y. Xu, T. Xu, Y. Guo, W. Liu and J. Wang, *Sep. Purif. Technol.*, 2023, **312**, 123433.
26 Y. Guo, H. Wu, S. Guo and J. Qiu, *Sep. Purif. Technol.*, 2022, **302**, 122163.
27 L. Wang, G. Xi, Z. Chen, Q. Wang, J. Liu, R. Zhang, T. Jia and X. Zhao, *J. Solid State Chem.*, 2023, **324**, 124070.
28 A. Ahmad, A. S. qureshi, L. Li, J. Bao, X. Jia, Y. Xu and X. Guo, *Colloids Surf., B*, 2016, **143**, 490–498.
29 F. Ali, S. B. Khan, T. Kamal, Y. Anwar, K. A. Alamry and A. M. Asiri, *Chemosphere*, 2017, **188**, 588–598.
30 K. Chu, X.-h. Wang, Y.-b. Li, D.-j. Huang, Z.-r. Geng, X.-l. Zhao, H. Liu and H. Zhang, *Mater. Des.*, 2018, **140**, 85–94.
31 N. Rani, K. Khurana and N. Jaggi, *Surf. Interfaces*, 2021, **27**, 101492.
32 X. Zhao, Y. Tang, J. Wang, Y. Li, D. Li, X. Zuo and H. Yang, *ACS Appl. Mater. Interfaces*, 2023, **15**, 49132–49145.
33 J. Li, Y. Jing, X. Zhou, J. Mao, Y. Chen, H. Sun, X. Deng and C. Gao, *Int. J. Energy Res.*, 2021, **45**, 20132–20142.
34 C. Pan, X. Li, G. Fan, H. Yang, Y. Long and F. Wu, *Arabian J. Chem.*, 2023, **16**, 105051.
35 M. Zhao, Y. Zhu, Y. Pan, Y. Wang, T. Xu, X. Zhao, T. Jia, Z. Zhang and Z. Chen, *ACS Appl. Energy Mater.*, 2022, **5**, 15758–15767.
36 G. Chen, N. Zhang, N. Li, L. Yu and X. Xu, *Adv. Mater. Interfaces*, 2019, **7**, 1901715.
37 H. Sang, C. Tang, K. Ma and X. Li, *J. Water Process Eng.*, 2023, **56**, 104461.
38 J. Wang, M. Sun, C. Liu, Y. Ye, M. Chen, Z. Zhao, Y. Zhang, X. Wu, K. Wang and Y. Zhou, *Adv. Mater.*, 2023, **35**, e2212258.
39 I. Zaaroura, S. Harmand, J. Carlier, M. Toubal, A. Fasquelle and B. Nongaillard, *Appl. Therm. Eng.*, 2021, **183**, 116203.
40 F. Zheng, Y. Zhang, L. Dong, D. Zhao, R. Feng, P. Tao, W. Shang, B. Fu, C. Song and T. Deng, *Nanoscale*, 2021, **13**, 20521–20530.
41 T. Li, M. Lin, H. Lu, Y. Chen, C. Zhang and H. Qi, *J. Environ. Chem. Eng.*, 2023, **11**, 109788.
42 M. Shang, S. Xu, J. Li, H. Sun, J. Peng, S. Wang and M. Zhang, *Energy Technol.*, 2021, **10**(2), 2100805.
43 W.-m. Zhang, J. Yan, Q. Su, J. Han and J.-f. Gao, *J. Colloid Interface Sci.*, 2022, **612**, 66–75.
44 C. Ge, D. Xu, H. Du, Z. Chen, J. Chen, Z. Shen, W. Xu, Q. Zhang and J. Fang, *Adv. Fiber Mater.*, 2022, **5**, 791–818.
45 J. Zhao, Z. Liu, S. C. Low, Z. Xu and S. H. Tan, *Adv. Fiber Mater.*, 2023, **5**, 1318–1348.
46 W. Chong, R. Meng, Z. Liu, Q. Liu, J. Hu, B. Zhu, D. K. Macharia, Z. Chen and L. Zhang, *Adv. Fiber Mater.*, 2023, **5**, 1063–1075.
47 H. Li, C. Xue, W. Cheng, L. Gao, X. Wang, H. Wei, H. Nan, G. Wang and H. Lin, *Prog. Org. Coat.*, 2021, **160**, 106526.
48 J. Li, Y. Li, S. Niu and N. Li, *Ultrason. Sonochem.*, 2017, **36**, 277–285.
49 X. Li, T. Liu, D. Wang, Q. Li, Z. Liu, N. Li, Y. Zhang, C. Xiao and X. Feng, *ACS Appl. Mater. Interfaces*, 2018, **10**, 21672–21680.
50 C. Zhou, H. Li, J. Lin, K. Hou, Z. Yang, P. Pi, S. Xu, X. Wen and J. Cheng, *J. Phys. Chem. C*, 2017, **121**, 19716–19726.
51 X. Fan, X. Qiu, L. Lu and B. Zhou, *Sol. Energy Mater. Sol. Cells*, 2021, **223**, 110948.
52 L. Han, Y.-N. Hao, X. Wei, X.-W. Chen, Y. Shu and J.-H. Wang, *ACS Biomater. Sci. Eng.*, 2017, **3**, 3230–3235.
53 H. Li, Y. Wang, J. Huang, Y. Zhang and J. Zhao, *Electrochim. Acta*, 2017, **225**, 443–451.
54 G. M. Neelgund, A. Oki, S. Bandara and L. Carson, *J. Mater. Chem. B*, 2021, **9**, 1792–1803.
55 J. A. Bush, J. Vanneste, E. M. Gustafson, C. A. Waechter, D. Jassby, C. S. Turchi and T. Y. Cath, *J. Membr. Sci.*, 2018, **554**, 366–377.
56 H. Li, H. Wen, J. Li, J. Huang, D. Wang and B. Z. Tang, *ACS Appl. Mater. Interfaces*, 2020, **12**, 26033–26040.
57 Z. Liu, H. Song, D. Ji, C. Li, A. Cheney, Y. Liu, N. Zhang, X. Zeng, B. Chen, J. Gao, Y. Li, X. Liu, D. Aga, S. Jiang, Z. Yu and Q. Gan, *Global chall.*, 2017, **1**, 1600003.
58 S. Song, H. Kim, C. Kang and J. Bae, *Nanomaterials*, 2023, **13**, 1948.
59 Z. Tang, A. George, A. Winter, D. Kaiser, C. Neumann, T. Weimann and A. Turchanin, *Chem.–A Euro. J.*, 2020, **26**, 6473–6478.
60 Y. Xie, A. Riedinger, M. Prato, A. Casu, A. Genovese, P. Guardia, S. Sottini, C. Sangregorio, K. Miszta, S. Ghosh, T. Pellegrino and L. Manna, *J. Am. Chem. Soc.*, 2013, **135**, 17630–17637.
61 S. Hu, J. Shi, B. Luo, C. Ai and D. Jing, *J. Colloid Interface Sci.*, 2022, **608**, 2058–2065.
62 K. Chen, Y. Shi, P. Shu, Z. Luo, W. Shi and F. Guo, *Chem. Eng. J.*, 2023, **454**, 140268.
63 C. Du, B. Yan and G. Yang, *Nano Energy*, 2020, **76**, 105052.
64 S. Lu, F. Liu, P. Qiu, M. Qiao, Y. Li, Z. Cheng, N. Xue, X. Hou, C. Xu, Y. Xiang, F. Peng and Z. Guo, *Chem. Eng. J.*, 2020, **379**, 122285.
65 X. Sun, Y. Shi, J. Lu, W. Shi and F. Guo, *Appl. Surf. Sci.*, 2022, **606**, 154960.
66 Y. Shi, L. Li, Z. Xu, F. Guo and W. Shi, *Chem. Eng. J.*, 2023, **459**, 141602.
67 J. Lu, Y. Shi, Z. Chen, X. Sun, H. Yuan, F. Guo and W. Shi, *Chem. Eng. J.*, 2023, **453**, 139826.
68 X. Tan, Y. Cheng and S. Wang, *Int. J. Therm. Sci.*, 2022, **179**, 107567.